Mechanisms of Li^+ diffusion in crystalline γ- and β-Li_3PO_4 electrolytes from first principles

Yaojun A. Du* and N. A. W. Holzwarth†
Department of Physics, Wake Forest University, Winston-Salem, North Carolina 27109, USA
(Received 6 July 2007; revised manuscript received 19 September 2007; published 15 November 2007)

Recently, there has been significant interest in developing solid-state lithium ion electrolytes for use in batteries and related technologies. We have used first-principles modeling techniques based on density-functional theory and the nudged elastic band method to examine possible Li ion diffusion mechanisms in idealized crystals of the electrolyte material Li_3PO_4 in both the γ and β crystalline forms, considering both vacancy and interstitial processes to find the migration energies E_m. We find that interstitial diffusion via an interstitialcy mechanism involving the concerted motion of an interstitial Li ion and a neighboring lattice Li ion may provide the most efficient ion transport in Li_3PO_4. Ion transport in undoped crystals depends on the formation of vacancy-interstitial pairs requiring an additional energy E_f, which results in a thermal activation energy $E_A=E_m+E_f/2$. The calculated values of E_A are in excellent agreement with single crystal measurements on γ-Li_3PO_4. Our results examine the similarities and differences between the diffusion processes in the γ and β crystal structures. In addition, we analyze the zone center phonon modes in both crystals in order to further validate our calculations with experimental measurements and to determine the range of vibrational frequencies associated with Li ion motions which might contribute to the diffusion processes.

DOI: 10.1103/PhysRevB.76.174302 PACS number(s): 82.45.Gj, 82.47.Aa, 71.15.Pd, 71.15.Nc

I. INTRODUCTION

In batteries and related technologies, electrolyte materials must be permeable to Li ions (Li^+) and impermeable to electrons. Because of their advantages,[1] solid electrolytes are being developed to replace liquid and polymer electrolytes and for new applications such as microelectronic devices. In particular, the LiPON electrolyte material based on Li_3PO_4 was developed at Oak Ridge National Laboratory.[2–5] Because of its chemical and physical stability, it can be reliably made into very thin films for a variety of applications.[1]

There has been considerable experimental work focused on measuring the ionic conductivity in crystalline Li_3PO_4 (Refs. 4 and 6–8) and in thin film Li_3PO_4.[4,9] On the other hand, experiment alone cannot determine the detailed atomistic mechanisms of Li ion diffusion in these materials. In our previous work,[10] we used first-principles modeling techniques to examine diffusion processes for Li ions in idealized crystals of γ-Li_3PO_4, finding quantitative and qualitative agreement with some of the experimental measurements. In this work, we present details of these simulations, extending our study to include the β-Li_3PO_4 crystalline form. In addition, we consider the effects of the form of the exchange-correlation functional on the simulation results, and also use comparison with experimental phonon measurements to assess the physical validity of our modeling methods.

The outline of the paper is as follows. Section II details the calculational methods used in this work. Section III describes the crystal structures of γ-Li_3PO_4 and β-Li_3PO_4. Results of the computed lattice parameters, electron densities of states, and the Raman spectra are presented in this section. In Sec. IV, ion diffusion via vacancy mechanisms is considered, while interstitial mechanisms are considered in Sec. V. The formation energy for vacancy-interstitial pairs is presented in Sec. VI, allowing us to compare our results with experimental studies on single crystals. In Sec. VII, our results are summarized and compared with the literature. Additional details of our phonon analyses are presented in the Appendix.

II. CALCULATIONAL METHODS

The calculations performed in this study were based on density-functional theory[11,12] and were primarily carried out using the QUANTUM ESPRESSO (PWSCF) package[13] and the ultrasoft pseudopotential formalism of Vanderbilt.[14] The pseudopotentials for Li, P, and O were constructed using the USPP code[14] and tested for agreement with calculations using other methods and codes.[15,16] For most of the calculations, the form of the exchange-correlation functional was chosen to be the local density approximation (LDA),[17] although some calculations were performed using the generalized gradient approximation (GGA).[18]

The calculations for single unit cells of the perfect crystals were performed using plane wave expansions for pseudo-wave-functions with wave vectors $|\mathbf{k}+\mathbf{G}|^2 \leq 64$ Ry. The Brillouin zone integrals were performed using a Monkhorst-Pack[19] sampling scheme within partitions of length 0.16 $bohr^{-1}$ or smaller in each direction. Lattice parameters and atomic positions were optimized using variable cell optimization techniques[20] as implemented in the PWSCF code. The zone center phonon frequencies and their corresponding vibrational modes were obtained by calculating the dynamical matrix using density-functional perturbation theory[21] as implemented in the PWSCF code. Convergence tests show that the lattice constants are converged to ±0.02 Å and that the computed phonon frequencies are converged within ±5 cm^{-1}. For convenience, the partial densities of states were evaluated using the PWPAW code,[22,23] which is based on the projector augmented wave formalism developed by Blöchl.[24] The evaluation of the partial densities of states uses a Gaussian shape function to replace the delta function:

$$N^a(E) \equiv \frac{2}{\sqrt{\pi}\Delta} \sum_{n\mathbf{k}} f^a_{n\mathbf{k}} W_{\mathbf{k}} e^{-(E-E_{n\mathbf{k}})^2/\Delta^2}. \quad (1)$$

Here, the factor of 2 is due to spin degeneracy, the factor $W_{\mathbf{k}}$ denotes the Brillouin zone weighting factor, and the smear-

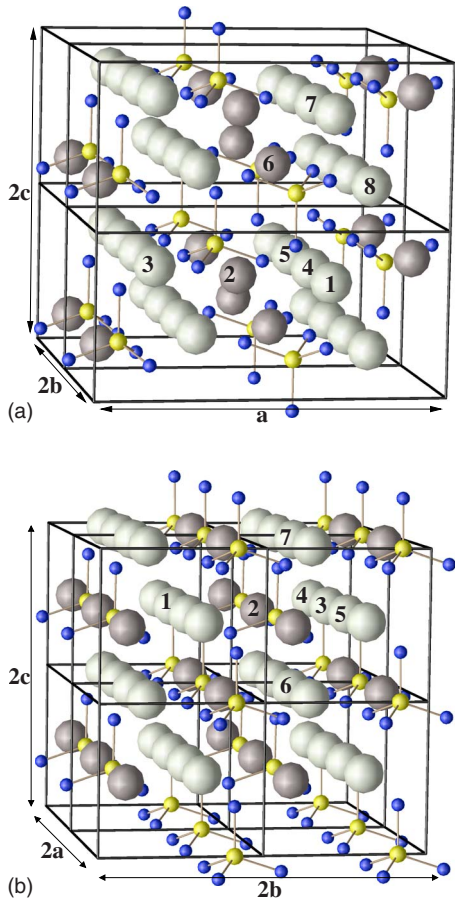

FIG. 1. (Color online) Ball and stick drawing of the equilibrium structures of the (a) γ-Li_3PO_4 and (b) β-Li_3PO_4 supercells used in the simulations. The PO_4 groups are indicated with bonded yellow and blue spheres. Li ions are indicated by light and dark gray spheres, representing the crystallographically distinct sites. The number labels on some of the Li sites are used in Sec. IV to describe vacancy diffusion.

ing parameter was chosen to be $\Delta=0.1$ eV. The factor $f^a_{n\mathbf{k}}$ denotes the charge within a sphere about atom a, with the radius taken to be 1.6, 1.5, and 1.4 bohr for Li, P, and O, respectively, for each state of band index n and wave vector $\mathbf{k}$. Comparing the PWSCF and PWPAW results, we found the total energy differences between perfect crystal structures to be within 0.002 eV.

Li ion migration simulations were carried out using the fixed volume supercells shown in Fig. 1 for the γ and β structures. For these large supercell simulations, the plane wave cutoff was chosen to be $|\mathbf{k}+\mathbf{G}|^2 \leq 30$ Ry and a single $\mathbf{k}$ point at the corner $(\frac{1}{2},\frac{1}{2},\frac{1}{2})$ was used to approximate the Brillouin zone integrals. Convergence tests show that the relative energies are accurate within 0.01 eV. Interstitial (vacancy) defects were simulated by adding (removing) a Li ion from the 128 atom supercell. The resulting supercells containing +1 (−1) excess electrons were compensated with a uniform background charge for the purpose of calculating the Coulomb interactions.

In this work, estimates for the migration energies E_m for Li ion diffusion were calculated using the "nudged elastic band"[25–27] method (NEB) as implemented in the PWSCF code. The basic assumptions of this approach[26] are that the diffusion is slow enough so that the processes are well described by Boltzmann statistics and so that the diffusion rate is controlled by processes which pass through harmonic regions of the potential energy surface near minima and saddle points, which represent transition states of the system. The computational effort is, thus, focused on finding the saddle points of the potential energy surfaces between local minimum energy configurations. For each of the diffusion paths considered, we find a series of steps characterized by pairs of local minimum energy configurations. The search for the saddle point is implemented by assuming several intermediate "images" between each pair of local minima. Each of the images is relaxed until the forces perpendicular to the minimum energy path are less than 0.03 eV/Å. The energies between each pair of local minima determined by interpolating between the energies of the images. We estimate that the accuracy of this interpolation allows us to estimate the saddle point energy barrier between each pair of local minima within 0.05 eV.

For example, consider an isolated ionic hopping step from a quasiequilibrium state q over a saddle point barrier b at temperature T. The conductivity contribution σ_{qb} from this process can be described by an Arrhenius equation[28,29]

$$\sigma_{qb}T = K_{qb}n_q e^{-(E_b-E_q)/k_BT} \quad \text{where } n_q = ne^{-E_q/k_BT}, \tag{2}$$

where k_B denotes the Boltzmann constant and K_{qb} denotes a temperature independent constant. Here, E_q represents the quasiequilibrium energy and E_b represents the barrier height for the saddle point, both measured relative to the lowest energy configuration of the path whose ion concentration is denoted by n. This expression assumes that a Boltzmann distribution of ions in the quasiequilibrium state q is developed due to hops from and to adjacent local minima. The conductivity contribution for this step, described by Eq. (2), thus reduces to the simple exponential form

$$\sigma_{qb}T = K_{qb}ne^{-E_b/k_BT}. \tag{3}$$

The observed macroscopic ionic conductivity within the crystal will, in general, involve one or more steps such as described in Eq. (3). It is reasonable to argue that the macroscopic ionic conductivity is dominated by the hopping step involving the largest barrier in the path so that the computed migration energy of a given path is $E_m=\max(E_b)$. In other words, the NEB results determine E_m as the energy difference between the lowest potential minimum and highest potential saddle point along the diffusion path. The macroscopic Arrhenius equation

$$\sigma T = Kne^{-E_m/k_BT}, \tag{4}$$

where K is a temperature independent constant appropriate to the migration path, can then be used to relate our simulation results to temperature dependent conductivity measurements. In practice, there may be several possible migration paths to describe conduction along any given crystallographic axis, resulting in alternative values of E_m. Of those values, the smallest values of E_m correspond to the largest conductivities and are the focus of the present work. A more detailed analy-

sis of the ionic processes would be needed to extend consideration beyond the simple exponential form of Eq. (4).

In order to further characterize each image of the diffusion path, it is convenient to define a "configuration coordinate," as a measure of the ion displacement at an image (I) relative to its position at the initial position (i). Using quantities calculated within the PWSCF code and other NEB implementations,[30] x_{iI} is chosen to be

$$x_{iI} = \Delta X_{if} \frac{u_{iI}}{u_{if}} \quad \text{where } u_{iI} \equiv \sum_{J=i+1}^{I} d_{JJ-1} \tag{5}$$

and where

$$d_{JJ-1} \equiv \left| \sum_{a} (\mathbf{R}_J^a - \mathbf{R}_{J-1}^a) \right|. \tag{6}$$

Here, $\mathbf{R}_J^a$ denotes the atomic position of the ath atom of the supercell in the Jth image and ΔX_{if} denotes the physical displacement between the initial and final vacancy or interstitial sites of a diffusion step measured for the perfect crystal. The distance d_{JJ-1} measures the length of the $3N$ dimensional displacement vector representing the motion of the N ions of the supercell between consecutive images, while u_{iI} measures the accumulated displacements of the Ith image relative to the initial configuration. The scaled configuration coordinate x_{iI} would represent the physical displacement of an ion or vacancy from image to image if only one ion were moving during the process. In the energy path diagrams shown in Figs. 5, 6, 8, and 9, x_{iI} is plotted on the horizontal axis in order to facilitate the comparison of consecutive diffusion steps of a given migration path. In Figs. 5 and 8, ΔX_{if} is taken from experimental data in order to plot the LDA and GGA results on the same scale. In Fig. 6 and 9, ΔX_{if} is taken from the LDA simulations.

Visualizations of the structures were obtained using XCRYSDEN (Ref. 31) and OPENDX (Ref. 32) softwares.

III. CRYSTALLINE PROPERTIES OF Li_3PO_4

A. Structural parameters

Experimentally, there are two well-characterized crystalline forms of Li_3PO_4 which are labeled β and γ.[4,33–35] An α form is mentioned in the literature,[36] but its crystal structure has not been completely determined. The β form has been shown to be energetically more stable than the γ form,[37] but it can irreversibly transform to the γ form at temperatures in the range of 400–600 °C.[9,36,38] At room temperature, it has been shown that the γ structure irreversibly transforms to the β form at pressures in the range of 120–230 kbar.[39] Both the β and γ forms of Li_3PO_4 have been observed and measured at liquid nitrogen temperature and room temperature by several experimental groups, while activated transport measurements have been mainly carried out on the γ form.

Crystalline γ-Li_3PO_4 has the orthorhombic *Pnma* structure (No. 62).[40] Figure 1(a) shows a ball and stick drawing of four unit cells of the ideal crystal. The Li ions are located on two crystallographically different sites indicated with different shadings in the figure. Using the Wyckoff labels, the d site accounts for eight equivalent atomic sites and the c site accounts for four equivalent atomic sites per unit cell. On the other hand, crystalline β-Li_3PO_4 has the orthorhombic $Pmn2_1$ structure (No. 31).[40] Figure 1(b) shows a similar drawing of eight unit cells of the ideal crystal. Its two crystallographically distinct Li sites are also indicated with different shadings in the figure. Using the Wyckoff labels, the b site accounts for four equivalent atomic sites and the a site accounts for two equivalent atomic sites per unit cell. As shown in Fig. 1, the **a**, **b**, and **c** axes in the γ form are similar to the $2\times$**b**, **a**, and **c** axes in the β form.[41] Both structures show similar arrangements of the Li ions, while the alignments of the phosphate groups differ. In the β structure, all of the phosphate groups are oriented in the same way relative to the **c** axis, while in the γ structure, half of the phosphate groups have the opposite orientation.

TABLE I. Lattice constants and fractional atomic coordinates of inequivalent atomic positions for γ-Li_3PO_4, comparing LDA and GGA simulation results with the experimental measurements of Ref. 35.

		LDA	GGA	Expt.
a (Å)		10.33	10.58	10.490
b (Å)		6.01	6.17	6.120
c (Å)		4.84	4.99	4.9266
Li(d)	x	0.164	0.164	0.1639
	y	0.502	0.502	0.5013
	z	0.305	0.303	0.3013
Li(c)	x	0.423	0.425	0.4237
	y	0.75	0.75	0.75
	z	0.201	0.202	0.2056
P(c)	x	0.412	0.412	0.41151
	y	0.25	0.25	0.25
	z	0.310	0.308	0.30878
O(d)	x	0.341	0.341	0.34167
	y	0.040	0.043	0.04289
	z	0.205	0.205	0.2057
O(c)	x	0.053	0.051	0.05042
	y	0.25	0.25	0.25
	z	0.296	0.297	0.2937
O(c)	x	0.088	0.089	0.08964
	y	0.75	0.75	0.75
	z	0.130	0.122	0.1223

Tables I and II list the lattice parameters and the fractional coordinates of the inequivalent atoms for the γ and β structures, showing that the lattice constants are calculated to be approximately 2% smaller than experiment using LDA and approximately 1% larger than experiment using GGA, as is consistent with our experience in density-functional studies of similar materials.[16] The experimental measurements[4,33–35] vary less than 1% among themselves. The calculated fractional atomic positions are insensitive to the form of the

TABLE II. Lattice constants and fractional atomic coordinates of inequivalent atomic positions for β--Li_3PO_4, comparing LDA and GGA simulations with experimental results of Ref. 34.

		LDA	GGA	Expt.
b (Å)		5.15	5.29	5.2394
a (Å)		6.01	6.16	6.1150
c (Å)		4.76	4.91	4.8554
Li(b)	y	0.328	0.327	0.328
	x	0.247	0.247	0.248
	z	0.993	0.993	0.986
Li(a)	y	0.838	0.845	0.843
	x	0.5	0.05	0.5
	z	0.992	0.993	0.989
P(a)	y	0.827	0.824	0.824
	x	0	0	0
	z	0	0	0
O(b)	y	0.685	0.686	0.687
	x	0.211	0.209	0.208
	z	0.893	0.894	0.896
O(a)	y	0.112	0.105	0.105
	x	0	0	0
	z	0.896	0.899	0.900
O(a)	y	0.178	0.181	0.181
	x	0.5	0.5	0.5
	z	0.825	0.819	0.817

exchange-correlation functional and generally agree with the experimental values of the fractional coordinates within ±0.008. The optimized energy results find $E_\gamma - E_\beta = 0.03$ eV per Li_3PO_4 for the LDA calculations and $E_\gamma - E_\beta = 0.01$ eV per Li_3PO_4 for the GGA calculations. Although we do not know of experimental measurements of these relative energies, the sign (indicating that the β structure is the more stable) is consistent with differential thermal analysis measurements.[37]

B. Densities of states

The partial densities of states calculated using the LDA exchange-correlation functional in Fig. 2 show that the two crystals have very similar density of states profiles, with the β form showing slightly smaller bandwidths than those of the γ form. As found in other phosphate materials,[15,16,42] the lowest bands correspond to the O $2p\sigma$ bonds with the P $3s$ states (near −7 eV) and O $2p\sigma$ bonds with the P $3p$ states (near −5 eV). The upper portion of the valence band has primarily O $2p\pi$ character relative to the P-O bonds. The states in the range $-3 \leqslant E \leqslant -1$ eV have a small hybridization with the P $p\pi$ states, while the states at the top of the valence band $-1 \leqslant E \leqslant 0$ eV have negligible admixture of P contributions. Throughout the valence band, there is a small

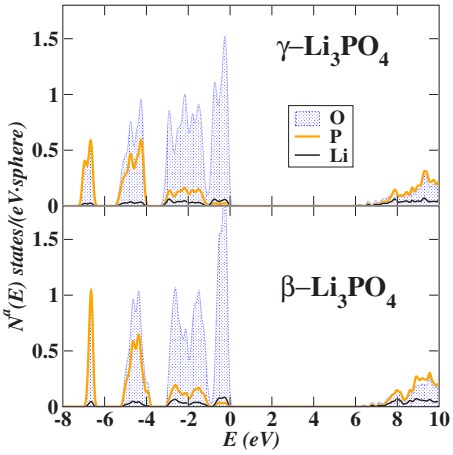

FIG. 2. (Color online) Partial densities of states $\langle N^a(E) \rangle$ for Li_3PO_4 comparing results for the γ and β structures, calculated using Eq. (1) and averaging over all spheres within the unit cell for each atomic species. The zero of energy is taken as the top of the highest occupied valence state.

contribution from the Li $2s$ states. The band gaps for both materials is calculated to be 6 eV, which, not surprisingly, is 2 eV smaller than the 8 eV band gap measured[43] for γ-Li_3PO_4. The shapes of the partial density of states plots for the γ structure are consistent with results of Xu *et al.*[44]

C. Zone center phonon modes

There have been several reports of experimental measurements of Raman and infrared absorption spectra of crystalline Li_3PO_4 (Refs. 36, 39, 43, and 45–47); therefore, our simulations of the zone center phonon modes serve as a validity check for our modeling as well as provide insight into Li ion motions in these crystals in the harmonic regime. Figures 3 and 4 show the spectra of Raman active modes calculated using the LDA and GGA exchange-correlation functions in comparison with various experimental measurements

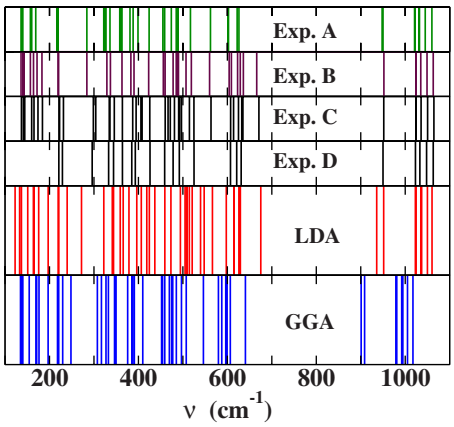

FIG. 3. (Color online) Spectrum of Raman active modes of γ-Li_3PO_4, comparing experimental results (A–D) corresponding to Refs. 45 and 43 (at room temperature) and Refs. 43 and 36 (at liquid nitrogen temperature), respectively, to the results of the LDA and GGA simulations.

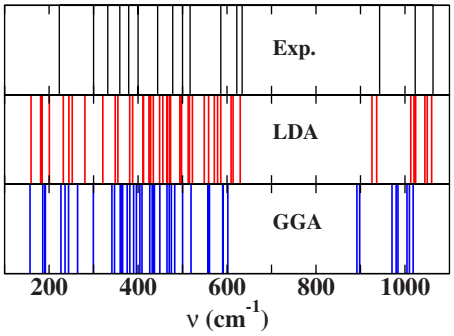

FIG. 4. (Color online) Spectrum of Raman active modes of β-Li_3PO_4, comparing experimental results corresponding to Ref. 36 (at liquid nitrogen temperature) to the results of the LDA and GGA simulations.

for the γ and β structures, respectively. Comparing the experimental spectra among themselves, we see that there is considerable variation in the results besides variations attributed to temperature effects. For example, Harbach and Fischer[43] reported a very low intensity mode at 670 cm^{-1}, attributed to primarily a PO_4 motion, shown in Fig. 3 as Exp. B and C for the room temperature and liquid nitrogen temperature measurements, respectively. None of the other experiments reports that mode. Comparing the general features of the Raman spectra for both the γ and β structures, we conclude that the LDA simulations have better agreement with experiment than do the GGA simulations. This is most apparent for frequencies $\nu > 900$ cm^{-1}, which correspond to internal vibrations of the PO_4 tetrahedra. In this region of the spectrum, the LDA results are close to experiment, while the GGA results underestimate the frequencies by 5%. At lower frequencies, the comparison between simulation and experiment is more complicated. In general, the simulations have more modes than are seen experimentally. Some of these discrepancies are undoubtedly due to intensity effects which we did not estimate. Nevertheless, from this comparison, we are tempted to conclude that the LDA exchange-correlation form represents a better physical model of Li_3PO_4 than does the GGA form. For completeness, we quote GGA results when available.

From the eigenvalues and eigenvectors of the dynamical matrix, we are able to examine the vibrational modes of Li_3PO_4 as discussed in the Appendix; in particular, the general analysis of the vibrations for both the γ and β forms finds three general spectral regions. The low frequency region, $0 \leqslant \nu \leqslant 300$ cm^{-1}, corresponds to rigid motions of the PO_4 tetrahedra. The intermediate region, $300 \leqslant \nu \leqslant 700$ cm^{-1}, corresponds to significant motion of the Li ions. These motions are strongly coupled to motions of the PO_4 groups as well. It is likely that the modes in this intermediate region may play a role in ionic conductivity through their contributions to the prefactor K in Eq. (4). In the high frequency region, $900 \leqslant \nu \leqslant 1100$ cm^{-1}, the motion is primarily internal vibrations of the PO_4 tetrahedra. This analysis is generally consistent with the assessment of Mavrin *et al.*[45] on the basis of their Raman experiments. While the general form of the Raman spectra of the γ and β crystals is quite similar, their differences show that the vibrations of the PO_4 tetrahedra and their coupling to the Li ions are sensitive to the long range order of the crystals.

TABLE III. Energies (in eV) of metastable vacancy sites in Li_3PO_4 calculated using the supercells shown in Fig. 1. The Li site labels correspond to the Wyckoff (Ref. 40) notation. In each case, the lowest energy configuration is defined as zero.

	Energy	
Site	LDA	GGA
	γ-Li_3PO_4	
Li(d)	0.20	0.22
Li(c)	0.00	0.00
	β-Li_3PO_4	
Li(b)	0.17	
Li(a)	0.00	

IV. ION VACANCY MIGRATION SIMULATIONS

The ion vacancy migration studies were carried out using the supercells shown in Fig. 1. As seen from the figure, if a single Li ion is removed from the crystal, there are several neighboring Li ions which can hop into the vacancy site and contribute to three-dimensional diffusion in γ-Li_3PO_4 and β-Li_3PO_4. We have considered several possible diffusion paths along the three orthogonal lattice directions in both structures. In our previous work,[10] we studied the diffusion paths for γ-Li_3PO_4 using GGA simulations. In the present work, we focus on LDA simulations for the reasons discussed in Sec. III C and compare the vacancy migration paths in the γ and β structures.

For each of the Li_3PO_4 crystal structures, there are two crystallographically inequivalent Li sites and, consequently, two metastable vacancy sites. Taking the lower energy site as the reference, we list the relative energies of these sites in Table III. For the γ structure, a vacancy at a site of type d (in the Wyckoff[40] notation) has higher energy than a vacancy at a site of type c. For the β structure, a vacancy at a site of type b has higher energy than a vacancy at a site of type a. In each crystal, diffusion steps which involve these two different sites will therefore differ depending on the direction of the step [$\Delta E(d \rightarrow c) < \Delta E(c \rightarrow d)$ for the γ structure and $\Delta E(b \rightarrow a) < \Delta E(a \rightarrow b)$ for the β structure]. For each of the four types of vacancies, we have verified that the relaxed structures have densities of states very similar to those of the bulk crystals shown in Fig. 2, introducing no impurity states within the band gap which could deteriorate the electrolyte properties of these materials.

Figure 5 compares the Li ion vacancy diffusion paths for γ-Li_3PO_4 identified in our previous study[10] using the GGA exchange-correlation functional with those of the present work obtained using the LDA exchange-correlation functional. This comparison shows that the two results are qualitatively very similar; for the most part, the LDA results show higher migration barriers relative to those of the GGA re-

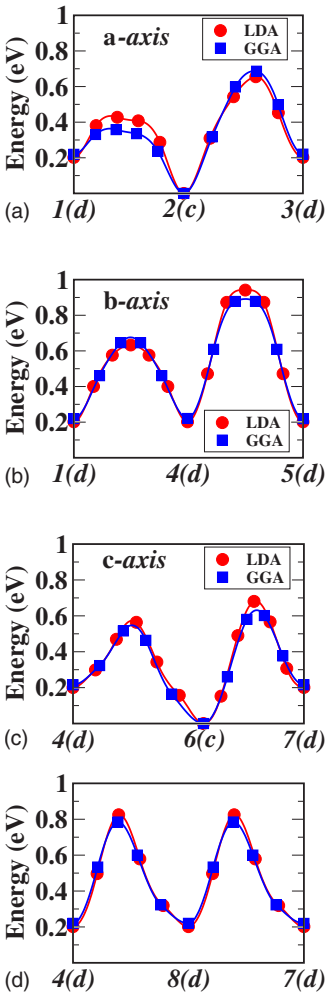

FIG. 5. (Color online) Diagram of LDA and GGA energy paths for **a**, **b**, and two alternative **c**-axis vacancy diffusions for γ-Li_3PO_4 plotted along the configuration coordinate defined in Eq. (5). The zero of energy is taken as the energy of a *c*-type Li ion vacancy as calculated from our supercell. (Note: In order to visualize the comparison of the LDA and GGA results, the value of ΔX_{if} was taken from the experimental data of Ref. 35.)

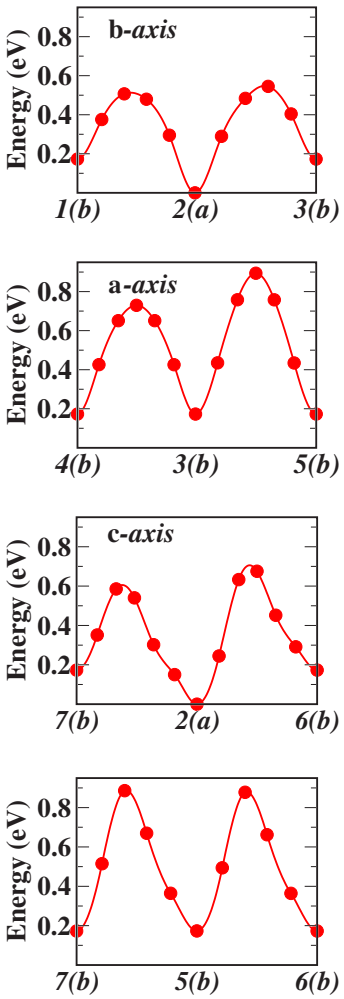

FIG. 6. (Color online) Diagram of LDA energy paths for **b**, **a**, and two alternative **c**-axis vacancy diffusions for β-Li_3PO_4, plotted along the configuration coordinate defined in Eq. (5). The zero of energy is taken as the energy of an *a*-type Li ion vacancy as calculated from our supercell ΔX_{if} was taken from our LDA calculations as reported in Table II.

sults. The quantitative differences are less than 0.1 eV for all of the vacancy paths considered.

Comparing the ideal supercells shown in Fig. 1 for the γ and β crystal structures, we find that Li ion placements in the two crystals are very similar if we relate the **a**, **b**, and **c** axes in the γ structure to the **b**, **a**, and **c** axes in the β structure. Figure 6 shows the Li ion vacancy diffusion paths for β-Li_3PO_4 calculated using the LDA exchange-correlation functional, analogous with those of Fig. 5.

The quantitative comparison between vacancy diffusion in γ-Li_3PO_4 and β-Li_3PO_4 is summarized in Table IV. Some of the detailed comparisons are very interesting. For diffusion along the **a** or **b** axis for the γ or β structures, respectively, the vacancy migration involves zigzag motions between inequivalent Li ion vacancy sites. For the γ structure, the two-step path involves vacancy sites $1(d) \leftrightarrow 2(c) \leftrightarrow 3(d)$ with a smaller energy barrier for the first step and a 0.66 eV barrier in LDA for the overall process. For the β structure, the corresponding two-step path involves vacancy sites $1(b) \leftrightarrow 2(a) \leftrightarrow 3(b)$ with a lower migration barrier for the first step and a 0.55 eV barrier for the overall process.

For diffusions along the **b** or **a** axis for the γ or β structures, respectively, diffusion can proceed in the direction along the axis, with hops between adjacent minimum energy sites of the same type. For the γ structure, the distance between the $1(d) \leftrightarrow 4(d)$ sites, is slightly smaller than the distance between the $4(d) \leftrightarrow 5(d)$ sites, and the migration barrier is slightly smaller for the shorter path, with a 0.74 eV barrier for the overall process. For the β structure, the distance between the $4(b) \leftrightarrow 3(b)$ sites is slightly smaller than the distance between the $3(b) \leftrightarrow 5(b)$ sites, and the migration barrier is slightly smaller for the shorter path, with a 0.72 eV barrier for the overall process. One might expect to find a low migration barrier diffusion along these axes, since recent simulations[48,49] for olivine ($LiFePO_4$) have found Li ion diffusion to occur mainly along one-dimensional channels of its **b** axis, which appear to have some structural similarities with the **b**-axis Li ion channels in γ-Li_3PO_4 and the correspond-

TABLE IV. Vacancy diffusion steps for γ- and β-Li_3PO_4 calculated with the LDA exchange-correlation functional. The step labels refer to the labels in Fig. 1 for the γ and β crystals. The distances (in Å) are given as the equivalent distances in a perfect crystal measured before relaxation. The migration energy E_m (in eV) corresponds to the maximum energy barriers between initial and final sites, hopping in either direction.

Axis	Step	Distance	E_m
	γ-Li_3PO_4		
a	$1(d)\leftrightarrow 2(c)$	2.91	0.43
	$2(c)\leftrightarrow 3(d)$	3.10	0.66
	$1(d)\leftrightarrow 2(c)\leftrightarrow 3(d)$	5.19	0.66
b	$1(d)\leftrightarrow 4(d)$	2.98	0.43
	$4(d)\leftrightarrow 5(d)$	3.03	0.74
	$1(d)\leftrightarrow 4(d)\leftrightarrow 5(d)$	6.01	0.74
c	$4(d)\leftrightarrow 8(d)$	2.97	0.62
	$4(d)\leftrightarrow 8(d)\leftrightarrow 7(d)$	4.84	0.62
	$4(d)\leftrightarrow 6(c)$	3.41	0.57
	$6(c)\leftrightarrow 7(d)$	2.60	0.68
	$4(d)\leftrightarrow 6(c)\leftrightarrow 7(d)$	4.84	0.68
	β-Li_3PO_4		
b	$1(b)\leftrightarrow 2(a)$	2.94	0.51
	$2(a)\leftrightarrow 3(b)$	3.03	0.55
	$1(b)\leftrightarrow 2(a)\leftrightarrow 3(b)$	5.15	0.55
a	$4(b)\leftrightarrow 3(b)$	2.97	0.56
	$3(b)\leftrightarrow 5(b)$	3.04	0.72
	$4(b)\leftrightarrow 3(b)\leftrightarrow 5(b)$	6.01	0.72
c	$6(b)\leftrightarrow 5(b)$	2.96	0.71
	$6(b)\leftrightarrow 5(b)\leftrightarrow 7(b)$	4.76	0.71
	$6(b)\leftrightarrow 2(a)$	2.93	0.71
	$2(a)\leftrightarrow 7(b)$	2.94	0.61
	$6(b)\leftrightarrow 2(a)\leftrightarrow 7(b)$	4.76	0.71

ing **a**-axis Li ion channels in β-Li_3PO_4. However, as shown in Table IV and in Figs. 5 and 6, the migration barriers for these paths are comparable to those of the other axes.

For vacancy diffusion along the **c** axis of both the γ and β structures, there are two possible zigzag paths. For the γ structure, the lowest migration energy that we have found occurs for the $4(d)\leftrightarrow 8(d)\leftrightarrow 7(d)$ path, which consists of two equivalent segments with a net barrier of 0.62 eV. For the β structure, both paths, $6(b)\leftrightarrow 5(b)\leftrightarrow 7(b)$ and $6(b)\leftrightarrow 2(a)\leftrightarrow 7(b)$, have a migration barrier of 0.71 eV.

In summary, using the LDA exchange-correlation functional, the NEB simulations of vacancy diffusion in γ-Li_3PO_4 find a slight anisotropy along the **a**, **b**, and **c** crystal axes with migration energy barriers of 0.66, 0.74, and 0.62 eV, respectively, compared with 0.69, 0.67, and 0.56 eV reported in our earlier study using the GGA exchange-correlation functional. Using the LDA exchange-correlation functional, the NEB simulations of vacancy diffusion in β-Li_3PO_4 find a slight anisotropy along the **b**, **a**, and **c** crystal axes with migration energy barriers of 0.55, 0.72, and 0.71 eV, respectively.

TABLE V. Parameters of some interstitial sites in γ-Li_3PO_4. The I_0, I_1, and II_0 sites are metastable, while the II^* site is an unstable saddle point. Energies are given in eV relative to the lowest energy interstitial site (I_0). The positions are given in terms of fractional coordinates (x,y,z) of the (a,b,c) unit cell lattice parameters listed in Table I.

	LDA		GGA	
Label	Energy	Position	Energy	Position
I_0	0.00	(0.30, 0.25, −0.01)	0.00	(0.30, 0.25, 0.00)
I_1	0.78	(0.28, 0.25, 0.57)	0.78	(0.28, 0.25, 0.59)
II_0	0.30	(0.52, 0.07, 0.56)	0.18	(0.52, 0.07, 0.57)
II^*	0.44	(0.50, 0.00, 0.50)	0.35	(0.50, 0.00, 0.50)

V. INTERSTITIAL ION MIGRATION SIMULATIONS

In our previous study[10] of interstitial Li ion migration in γ-Li_3PO_4, using the GGA exchange-correlation functional, we found several metastable interstitial sites and found that an "interstitialcy" mechanism,[29,50,51] involving the concerted motion of an interstitial Li ion and a neighboring Li ion of the host lattice, can provide the most efficient mechanism for migration between these metastable sites. In this work, we present the results of a similar study using the LDA exchange-correlation functional and also consider interstitial Li ion migration in the β crystalline form.

The interstitial ion migration studies were carried out using the supercells shown in Fig. 1. As shown in our previous work,[10] the γ form has two distinct void channels along the **c** axis, which we labeled *I* and *II*. In general, the *II*-type channels are characterized by having twice as many neighboring phosphate groups along the channel compared to the *I*-type channels. Table V lists the energies and positions of metastable interstitial sites in those channels, comparing the LDA and GGA results. Also listed in the table are the relative energy and position of an unstable saddle point labeled II^*,[10] which are important for the interstitial migration mechanism. A NEB simulation examining the configurations in the close vicinity of the II^* site confirms that it is a saddle point and not a higher order maximum energy configuration. Because of the *Pnma* crystal symmetry, there are several equivalent interstitial sites in each unit cell. The I_0, I_1, and II^* sites have a multiplicity of 4, while the II_0 sites have a multiplicity of 8. The β crystals have similar void channels which are shown in Fig. 7. The energies and positions of metastable interstitial sites for the corresponding *I*-type and *II*-type void channels are listed in Table VI. In contrast to the γ structure, for the β structure, the unstable saddle point analogous to II^* is not located at a high symmetry point and is not listed in Table VI. Because of the $Pnm2_1$ crystal symmetry, there are several equivalent interstitial sites within the unit cell. The I_0

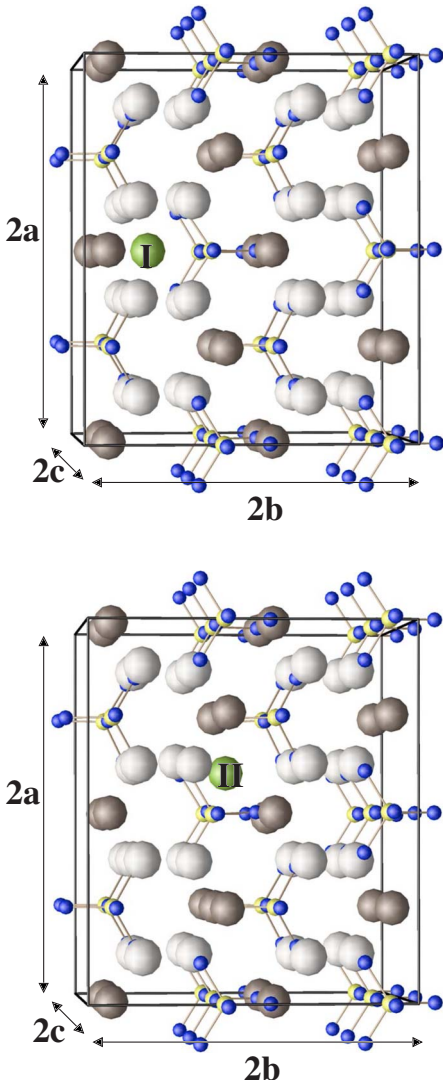

FIG. 7. (Color online) Ball and stick drawing of metastable interstitial Li ion configurations in β-Li_3PO_4 viwed along the **c** axis using the same conventions as Fig. 1, with the interstitial sites labeled I (top) and II (bottom) (green). These correspond to the I_0 and II_0 sites, respectively, as listed in Table VI.

and I_1 sites have a multiplicity of 2, while the II_0 and II_1 sites have a multiplicity of 4. The list of metastable interstitial sites given in Tables V and VI represents a general scan of reasonable trial geometries, undoubtedly, not an exhaustive

TABLE VI. Parameters of some metastable interstitial sites in β-Li_3PO_4. Energies are given in eV relative to the lowest energy interstitial site (I_0). The positions are given in terms of fractional coordinates (y,x,z) of the (b,a,c) unit cell lattice parameters listed in Table II.

Label	Energy	Position
I_0	0.00	(0.45, 0.00, 0.66)
I_1	0.30	(0.42, 0.00, 0.24)
II_0	0.38	(−0.07, 0.78, 0.64)
II_1	0.39	(0.00, 0.82, 0.64)

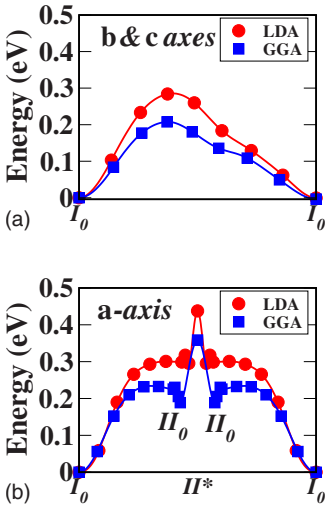

FIG. 8. (Color online) Diagram of LDA and GGA energy paths plotted along the configuration coordinate defined in Eq. (5) for interstitial diffusion in γ-Li_3PO_4 (top) along the **b** and **c** axes between adjacent I_0 configurations via an interstitialcy mechanism and (bottom) along the **a** axis between adjacent *I* and *II* channel sites using a combination of interstitialcy and direct-hop steps. The energy of the I_0 configuration was taken as the zero of energy. (Note: In order to visualize the comparison of the LDA and GGA results, the value of ΔX_{if} was taken from the experimental data of Ref. 35.)

list. For the lowest energy metastable interstitial configurations, we have verified that the relaxed structures have densities of states very similar to those of the bulk crystals shown in Fig. 2, introducing no impurity states within the band gap, which could deteriorate the electrolyte properties of these materials.

Figure 8 compares the interstitial Li ion diffusion paths for γ-Li_3PO_4 identified in our previous study[10] using the GGA exchange-correlation functional with those of the present work obtained using the LDA exchange-correlation functional. Similar to the vacancy migration studies, the interstitial migration results using LDA generally show higher barriers compared to the GGA results. The quantitative differences are approximately 0.1 eV or less for the paths considered.

For both the γ and β structures, we find that Li ion migration between channels of type *I* with an interstitialcy mechanism provides the most efficient transport along the **b** and **c** directions and along the **a** and **c** directions, respectively. For example, as shown in Fig. 8 and Table VII, for the γ structure, a net migration from the metastable I_0 interstitial site at (−0.30, 0.75, 0.99) to an equivalent I_0 (−0.20, 0.25, 0.49) site can efficiently occur via the concerted motion of the interstitial Li ion and a neighboring *d*-type Li ion of the host lattice. During this so-called interstitialcy process, an interstitial Li ion at an I_0 site kicks out and replaces a neighboring *d*-type Li of the host lattice, while the "kicked-out" Li ion takes an equivalent interstitial I_0 site. The NEB results using the LDA exchange-correlation functional indicate that the migration energy for this interstitialcy step is E_m =0.29 eV. Diffusion along the **b** and **c** axes for an interstitial ion in any *I*-type channel can, thus, be described as a series

TABLE VII. Interstitial diffusion steps for γ- and β-Li_3PO_4 calculated with the LDA exchange-correlation functional. The step labels refer to the metastable or saddle point configurations listed in Tables V and VI. The distances (in Å) are estimated as the equivalent distances between interstitial sites in a perfect crystal before relaxation. The migration energy E_m (in eV) is the maximum energy barrier between the initial and final configurations of the step.

Type	Step	Distance	E_m
	γ-Li_3PO_4		
Interstitialcy	$I_0 \leftrightarrow I_0$	4.0	0.29
Interstitialcy	$I_0 \leftrightarrow II_0$	3.3	0.30
Direct hop	$II_0 \leftrightarrow II^*$	0.5	0.14
	$I_0 \leftrightarrow II_0 \leftrightarrow II^* \leftrightarrow II_0 \leftrightarrow I_0$	7.0	0.44
	β-Li_3PO_4		
Interstitialcy	$I_0 \leftrightarrow I_0$	3.9	0.39
Interstitialcy	$I_0 \leftrightarrow II_0$	3.5	0.53
Direct hop	$II_0 \leftrightarrow II_1$	0.5	0.05
Interstitialcy	$II_1 \leftrightarrow I_0$	2.5	0.52
	$I_0 \leftrightarrow II_0 \leftrightarrow II_1 \leftrightarrow I_0$	6.0	0.53

of zigzag steps with this mechanism. This interstitialcy process is by far more efficient energetically than any of the other interstitial diffusion mechanisms we have considered, including direct hopping between I_0 and neighboring I_0 or I_1 sites. For the β structure, as shown in Fig. 9 and Table VII, we have found that diffusion between a metastable interstitial site I_0 at the position $(y,x,z)=(-0.45,0.50,0.16)$ and its

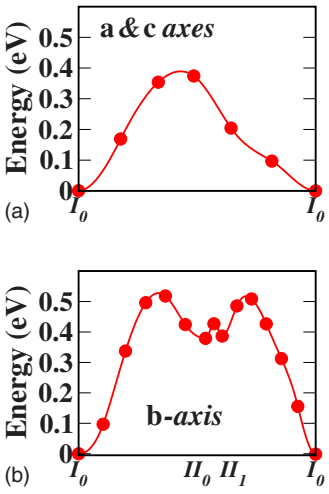

FIG. 9. (Color online) Diagram of LDA energy path plotted along the configuration coordinate defined in Eq. (5) for interstitial diffusion in β-Li_3PO_4 (top) along the **a** and **c** axes between adjacent I_0 configurations via an interstitialcy mechanism and (bottom) along the **b** axis between adjacent I and II channel sites using a combination of interstitialcy and direct-hop steps. The energy of the I_0 configuration was taken as the zero of energy. ΔX_{if} was taken from our LDA calculations as reported in Table II.

equivalent site at $(-0.55,0.00,-0.34)$ takes place most efficiently via an interstitialcy mechanism between interstitial Li ion and a neighboring b-type Li ion of the host lattice. During the interstitialcy process, an interstitial Li ion at an I_0 site kicks out and replaces a neighboring b-type Li of the host lattice, while the kicked-out Li ion takes an equivalent interstitial I_0 site. The NEB results indicate that the migration energy for this interstitialcy step is $E_m=0.39$ eV. Diffusion along the **a** and **c** axes for an interstitial ion in any I-type channel can, thus, be described as a series of zigzag steps with this mechanism.

In order for interstitial ions to diffuse along the **a** axis in the γ structure or the **b** axis in the β structure, both the I- and II-type void channels must be involved. For the γ structure, one possible mechanism involves the net motion of an interstitial ion at an I_0 site at $(x,y,z)=(0.30,0.25,0.99)$ diffusing to an equivalent I_0 site at (0.70, −0.25, −0.01) with an overall migration energy of 0.44 eV using the following three steps illustrated in Fig. 8 and Table VII. The first step involves the configurations $I_0 \leftrightarrow II_0$ with an energy barrier of 0.30 eV. In this step, an interstitial Li ion at an I_0 site (0.30, 0.25, 0.99) kicks a distorted neighboring c-type Li ion of the host lattice into a II_0 configuration at the interstitial site (0.52, 0.07, 0.56). The second step involves the configurations $II_0 \leftrightarrow II^* \leftrightarrow II_0$ with a relative barrier of 0.14 eV. This process takes place within the type II void channel, with the interstitial ion in the II_0 configuration performing a direct hop to an equivalent II_0 site at (0.48, −0.07, 0.44), passing over the saddle point configuration at II^* (0.50, 0.00, 0.50). The third step involves the configurations $II_0 \leftrightarrow I_0$. In this process, the Li ion at the interstitial II_0 site at (0.48, −0.07, 0.44) kicks out another distorted c-type Li ion of the host lattice into an I_0 configuration (0.70, −0.25, −0.01). It is worth noting that this mechanism has an inversion symmetry centered at the saddle point configuration II^* at the site (0.50, 0.00, 0.50). The overall migration barrier for this process is given by the energy of the saddle point at II^* relative to the metastable configuration at I_0 and is, therefore, $E_m=0.44$ eV. For the β structure, one possible path for interstitial diffusion along the **b** axis as illustrated in Fig. 9 and Table VII involves an interstitial ion at an I_0 site at $(y,x,z)=(0.45,0.00,0.66)$ diffusing to an equivalent I_0 site at $(-0.45,0.50,0.16)$ with an overall migration energy of $E_m=0.53$ eV. This process consists of three steps. The first step involves the configurations $I_0 \leftrightarrow II_0$ with a migration barrier of 0.53 eV. In this step, an interstitial Li ion at the initial I_0 site kicks a neighboring b-type Li ion of the host lattice into an II_0 configuration with the interstitial site (0.07, 0.28, 0.14). The second step involves the configurations $II_0 \leftrightarrow II_1$ with a relative migration energy barrier of $E_m=0.05$ eV. This process takes place within the type II void channel and involves the interstitial ion at the II_0 site performing a direct hop into the II_1. In contrast to the situation for the γ structure, for the β structure, the energy barrier of the saddle point is small and does not affect the overall migration barrier of the process. The last step involves the configurations $II_1 \leftrightarrow I_0$. In this process, the Li ion at the interstitial II_1 site kicks out another a-type Li ion of the host lattice into an I_0 configuration $(-0.45,0.50,0.16)$ with a migration barrier of $E_m=0.52$ eV.

In summary, using the LDA exchange-correlation functional, the NEB simulations of interstitial diffusion in

γ-Li_3PO_4 find the migration energy barriers along the **b** and **c** axes to be E_m=0.29 eV via an interstitialcy mechanism, and along the **a** axis to be E_m=0.44 eV via a combination of interstitialcy and direct-hop mechanisms. The corresponding results using the GGA exchange-correlation functional find these energies to be E_m=0.21 eV and E_m=0.35 eV, respectively. Correspondingly, using the LDA exchange-correlation functional, the NEB simulations of interstitial diffusion in β-Li_3PO_4 find the migration energy barriers along the **a** and **c** axes to be E_m=0.39 eV via an interstitialcy mechanism and along the **b** axis to be E_m=0.53 eV via a combination of interstitialcy and direct-hop mechanisms.

VI. FORMATION ENERGIES FOR VACANCY-INTERSTITIAL PAIRS OF INTRINSIC DEFECTS

By definition, in a perfect crystal, no vacancies or interstitial ions can exist, so that mobile species such as vacancies and interstitials must first be created before ion diffusion can occur. In real crystals, intrinsic defects (vacancy-interstitial pairs) are created thermally with a formation energy E_f. Using the supercells shown in Fig. 1 to relax the geometries of several initial guesses for defect geometries, we find the smallest defect formation energy to be $E_f \approx 1.7$ eV in γ-Li_3PO_4 using the LDA form of the exchange-correlation functional. In our previous work,[10] we found $E_f \approx 1.6$ eV using the GGA form. For β-Li_3PO_4, the smallest formation energy was found to be $E_f \approx 2.1$ eV using the LDA form. In all of these cases, the smallest vacancy-interstitial pair formation energy corresponds to the interstitial I_0 site as described in Tables V and VI and a next nearest neighbor vacancy at a *c*-type or an *a*-type Li site for the γ or β crystals, respectively. (Using an initial defect configuration with the I_0 interstitial site and its nearest neighbor vacancy site, we find that the system relaxes into its perfect crystal geometry.)

The formation energy affects the measured activation energy for ionic conductivity due to intrinsic defects.[29,51] Equation (4) shows the relationship of the concentration of mobile ions n to the ionic conductivity. For extrinsic defects, the concentration of mobile ions n is determined by the doping process and is independent of temperature so that the Arrhenius activation energy is $E_A \equiv E_m$. On the other hand, for intrinsic defects, the concentration of mobile ions n is determined by the formation of vacancy-interstitial pairs. Following the derivation in Ref. 51, we can assume that these defects are formed by a perfect crystal ion moving into an interstitial site, ensuring an equal number (n) of vacancies and interstitials with a formation energy E_f. If we assume that there is a thermal equilibrium between the number of vacancy and interstitial defects compared with the number of unvacant lattice sites and unoccupied interstitial sites, the concentration (n) of vacancies and interstitials is determined by a Boltzmann factor

$$n^2 \propto e^{-E_f/k_BT}. \tag{7}$$

Using this relation in Eq. (4), we find

$$\sigma \cdot T = K' e^{-(E_m+E_f/2)/k_BT} \equiv K' e^{-E_A/k_BT}, \tag{8}$$

so that for the case of intrinsic defects, the activation energy is given by

TABLE VIII. Activation energies E_A (in eV) for intrinsic Li ion defects in γ-Li_3PO_4 and β-Li_3PO_4, comparing experimental results of Ref. 8 with simulation results.

Crystal	Direction	E_A (Expt.)	E_A (LDA)	E_A (GGA)
γ-Li_3PO_4	**a**	1.23	1.3	1.2
	b	1.14	1.1	1.0
	c	1.14	1.1	1.0
β-Li_3PO_4	**b**		1.6	
	a		1.4	
	c		1.4	

$$E_A = E_m + E_f/2. \tag{9}$$

By using Eq. (9) for our simulations and assuming that the minimum energy processes dominate, we can estimate the anisotropic activation energies for ionic conductivity in Li_3PO_4. For conductivity in each lattice direction, we can compare the net migration barriers for the vacancy (Table IV) and interstitial (Table VII) mechanisms. In each case, the interstitial mechanisms have lower energy than the corresponding vacancy mechanisms. Combining these interstitial values of E_m with the minimum values of E_f quoted above, we estimate the activation energies for intrinsic defects listed in Table VIII. The calculated activation energies for γ-Li_3PO_4 agree very well with the single crystal measurements of Ivanov-Shitz *et al.*[8] Not only is there good numerical agreement, but also the fact that the activation energies for the **b** and **c** axes are the same can be understood. In Sec. V, we showed that interstitial diffusion along both of these axes can be described as a series of zigzag paths between *I*-type void channels via the same interstitialcy mechanism.

VII. SUMMARY AND CONCLUSIONS

Using the LDA exchange-correlation functional to simulate the zone center phonon modes of γ-Li_3PO_4 and β-Li_3PO_4, we found good agreement with experimental Raman and infrared measurements, particularly for the high frequency modes, while results using the GGA functional showed less good agreement. This leads us to suggest that the LDA results may represent a better simulation model of the Li_3PO_4 system. Analysis of the vibrational modes finds that the intermediate frequency range $300 < \nu < 700$ cm^{-1} (or $9 < f < 21$ THz) involves significant Li ion motions which are related to the "attempt" frequencies that determine the prefactors for ion diffusion.

Some of the main results of the Li ion diffusion simulations are as follows. Using density-functional theory and supercells with 16 Li_3PO_4 formula units, we identified a number of metastable vacancy and interstitial defect configurations which describe high probability intermediate states in Li ion diffusion in γ-Li_3PO_4 and β-Li_3PO_4. These metastable states do not contribute to electronic states within the energy gaps and, therefore, maintain the electrolyte properties of the materials. Using NEB methodology, we identified migration energy barriers, E_m, for transitions between

these metastable sites. Using the LDA exchange-correlation functional, the migration barriers for vacancy diffusion via a direct-hop mechanism were found to be 0.66, 0.74, and 0.62 eV along the **a**, **b**, and **c** axes, respectively, for the γ structure, and 0.55, 0.72, and 0.71 eV along the **b**, **a**, and **c** axes, respectively, for the β structure. Using the GGA exchange-correlation functional, the corresponding migration energy barriers were found to be 0.69, 0.67, and 0.56 eV along the **b**, **a**, and **c** axes, respectively, for the γ structure. Using the LDA functional, the migration barriers for interstitial ion diffusion via interstitialcy mechanism or a combination of interstitialcy and direct-hop mechanisms were found to be 0.29 and 0.44 eV along the **b** and **c** axes and along the **a** axis, respectively, for the γ structure, and 0.39 and 0.53 eV along the **a** and **c** axes and along the **b** axis, respectively, for the β structure. Using the GGA functional, the corresponding migration energy barriers were found to be 0.21 and 0.35 eV along the **b** and **c** axes and along the **a** axis, respectively, for the γ structure. These results indicate that the interstitial ion processes are considerably more efficient for ion transport compared with vacancy transport processes in these materials.

From the estimation of the formation energy E_f for vacancy-interstitial pair defects in a perfect crystal, we can estimate the activation energy for ion diffusion in crystalline Li_3PO_4 using the relation $E_A = E_m + E_f/2$. The results listed in Table VIII which use values of E_m from the interstitial mechanism compare very well with measurements[8] on single crystal γ-Li_3PO_4. The results are also in good agreement with measurements on polycrystalline samples,[4,6,7] where the activation energies are found to be $E_A = 1.1-1.3$ eV and where we assume that the samples had no significant concentration of extrinsic defects. The corresponding activation energies for the β crystalline form are 0.3 eV higher due to both higher migration energy barriers and a larger formation energy for the vacancy-interstitial pairs.

Quantitative comparison of our results with experiments on crystals with extrinsic defects is more difficult; however, we can make the following observations. In crystals prepared with a measurable number of extrinsic vacancies, the measured activation energies are considerably reduced. For example, Wang *et al.*[4] prepared a crystal with the measured stoichiometry of $Li_{2.88}PO_{3.73}N_{0.14}$, which has 4% Li vacancies per formula unit, with N substituting for some O ions and some additional O vacancies, approximately adjusted for charge neutrality. For this material, the activation energy was measured to be $E_A = 0.97$ eV, reduced by 0.27 eV from that of the pure material. On the other hand, this measured activation energy is much larger than the value of $E_m = 0.6-0.7$ eV calculated in our simulations of vacancy diffusion in the otherwise perfect γ-Li_3PO_4 crystal. Preliminary results of our further simulations on this system[52] indicate that O vacancies in the vicinity of Li vacancies tend to increase the migration energies of the Li vacancies. In future work, we also plan to consider the effects of N doping. Cluster calculations reported in the literature[53] find N to have a significant effect on migration barriers for Li ion vacancies.

On the basis of our modeling, we believe that the interstitialcy mechanism should provide the most efficient ion transport for Li_3PO_4-based materials. We note that an early study of Li_4SiO_4-Li_3PO_4 solid solutions[6] found that a Li_4SiO_4-Li_3PO_4 solid solution with a 0.4 mole fraction of Li_4SiO_4 had the lowest activation energy of $E_A = 0.5$ eV compared to $E_A = 1.3$ eV for pure Li_3PO_4. It is expected that introducing Li_4SiO_4 into the Li_3PO_4 lattice produces a significant concentration of Li interstitials, which may contribute to the reduction in activation energy. The complete story of this system is undoubtedly affected by the Si ions, but it is interesting to note that our computed migration barriers of interstitial Li ions in ideal γ and β-Li_3PO_4 crystals are computed to be 0.3–0.5 eV, which suggest that an interstitialcy mechanism may contribute to the ionic conductivity in the Li_4SiO_4-Li_3PO_4 solid solution materials.

ACKNOWLEDGMENTS

This work was supported by NSF Grants Nos. NSF DMR-0405456 and DMR-0427055, and benefited from discussions with R. E. Noftle, G. E. Matthews, W. C. Kerr, Ping Tang, and Xiao Xu at Wake Forest University, Richard Hennig at Cornell University, and Dallas Trinkle at the University of Illinois, as well as from helpful advice from Nancy J. Dudney of Oak Ridge National Laboratory. Computational results were obtained using the DEAC cluster, and benefited from storage hardware awarded to Wake Forest University through an IBM SUR grant.

APPENDIX: ANALYSIS OF PHONON MODES

The eigenvalues and eigenvectors of the dynamical matrices can be analyzed according to their group symmetries and their corresponding Raman and infrared transition matrix elements.[54] For γ-Li_3PO_4, which has 32 atoms per unit cell, there are 96 vibrational modes which decompose into the following irreducible representations:[43,45]

$$14A_g \oplus 10B_{1g} \oplus 14B_{2g} \oplus 10B_{3g} \oplus 10A_u \oplus 14B_{1u} \oplus 10B_{2u} \oplus 14B_{3u}. \quad \text{(A1)}$$

Symmetry analysis further finds[54,45] that the 48 modes with g character are Raman active, the 10 A_u modes and 3 zero frequency acoustic modes $(1B_{1u} \oplus 1B_{2u} \oplus 1B_{3u})$ are silent, while the 35 remaining $13B_{1u} \oplus 9B_{2u} \oplus 13B_{3u}$ modes are infrared active.

In addition to the symmetry analysis, it is also interesting to analyze the atomic motions associated with the modes. For γ-Li_3PO_4, there are six inequivalent atoms. Each phonon mode can be characterized by the magnitudes of the displacements for each of the inequivalent atoms. Using the Wyckoff site labels, we denote the magnitude of displacement of six inequivalent atoms Li(d), Li(c), P(c), O(d),

TABLE IX. Raman active vibrational modes of γ-Li_3PO_4 calculated using PWSCF and LDA exchange-correlation form. The symmetry assignment is based on the character tables given in Ref. 54. r is defined in Eq. (A2). The atomic assignment is based on $r_{thr}=0.9$ as explained in the text.

ν (cm^{-1})	Symmetry	Assignment	r
123	B_{3g}	PO_4	1.7
133	A_g	PO_4	2.2
137	B_{1g}	PO_4	2.3
151	A_g	PO_4	2.1
164	B_{1g}	PO_4	1.6
165	B_{2g}	PO_4	2.1
176	B_{3g}	PO_4	2.9
197	B_{2g}	PO_4	2.9
220	B_{3g}	PO_4	2.3
220	A_g	PO_4	2.2
240	B_{2g}	PO_4	2.4
272	B_{1g}	PO_4	3.0
322	A_g	Li	0.34
341	B_{2g}	Li	0.35
344	A_g	PO_4	1.0
359	B_{2g}	PO_4	0.96
366	B_{1g}	Li	0.53
379	B_{3g}	Li	0.58
396	B_{1g}	PO_4	0.95
406	A_g	Li	0.68
419	B_{3g}	Li	0.87
424	B_{2g}	Li	0.32
437	B_{1g}	Li	0.48
459	B_{3g}	Li	0.43
473	B_{2g}	Li	0.77
494	A_g	Li	0.67
505	B_{3g}	PO_4	0.90
509	A_g	Li	0.66
509	B_{1g}	Li	0.34
514	B_{2g}	PO_4	0.91
521	A_g	Li	0.54
540	B_{1g}	Li	0.83
548	B_{3g}	Li	0.87
566	B_{2g}	Li	0.89
598	A_g	PO_4	1.3
615	A_g	PO_4	0.99
615	B_{2g}	Li	0.64
626	B_{1g}	PO_4	1.8
629	B_{3g}	PO_4	1.2
675	B_{2g}	PO_4	1.0
936	A_g	PO_4	14
952	B_{2g}	PO_4	4.9
1023	A_g	PO_4	21
1024	B_{3g}	PO_4	14
1035	A_g	PO_4	23
1036	B_{2g}	PO_4	12
1050	B_{2g}	PO_4	13
1060	B_{1g}	PO_4	10

O(c), and O(c) by x^d_{Li}, x^c_{Li}, x^c_{P}, x^d_{O}, $x^{c'}_{\mathrm{O}}$, and $x^{c''}_{\mathrm{O}}$, respectively. The ratio of displacements between ions in the PO_4 tetrahedra and the Li ions can be defined as

$$r=\frac{\max(x^c_{\mathrm{P}},x^d_{\mathrm{O}},x^{c'}_{\mathrm{O}},x^{c''}_{\mathrm{O}})}{\max(x^d_{\mathrm{Li}},x^c_{\mathrm{Li}})}. \tag{A2}$$

In order make assignments for the mode character, it is convenient to define a threshold ratio r_{thr} such that the modes with $r\geq r_{thr}$ will be assigned as PO_4 modes, while the other modes with $r<r_{thr}$ will be assigned as Li modes. In this work, we chose $r_{thr}=0.9$ in order to ensure that 18 modes assigned to Li are Raman active as analyzed by Ref. 45.

The LDA computed phonon modes are listed in Table IX and Table X for the Raman active modes and infrared active and silent modes, respectively, including their symmetry labels and atomic assignments. Remarkably, the highest frequency mode is computed to be infrared active and exactly reproduces the experimental value of 1153 cm^{-1}.[46] There is generally good agreement between experiment and calculation for the high frequency Raman active modes, although there are some discrepancies in the symmetry assignments listed in Table IX with those determined from the Raman polarizations.[43,45]

For β-Li_3PO_4, there are 16 atoms per unit cell and 48 vibrational modes. These can be decomposed into the following irreducible representations:[54]

$$14A_1\oplus 10B_1\oplus 10A_2\oplus 14B_2. \tag{A3}$$

All these modes except for the three zero frequency acoustic modes ($A_1\oplus B_1\oplus B_2$) are Raman active and, except for the A_2 modes, are also infrared active. For the β structure, there are six inequivalent atoms in β-Li_3PO_4, resulting in six inequivalent atomic displacements for each phonon vibrational mode. Using the Wyckoff labels, we denote the magnitude of displacement of six inequivalent atoms Li(b), Li(a), P(a), O(b), O(a), and O(a) by x^b_{Li}, x^a_{Li}, x^a_{P}, x^b_{O}, $x^{a'}_{\mathrm{O}}$, and $x^{a''}_{\mathrm{O}}$, respectively. In analogy to Eq. (A2), the ratio of displacements between PO_4 tetrahedron and Li ion can be defined as

$$r=\frac{\max(x^a_{\mathrm{P}},x^b_{\mathrm{O}},x^{a'}_{\mathrm{O}},x^{a''}_{\mathrm{O}})}{\max(x^b_{\mathrm{Li}},x^a_{\mathrm{Li}})}. \tag{A4}$$

Again choosing $r_{thr}=0.9$, we can assign the atomic character of modes as listed in Table XI. In general, the comparison with experiment[36] is best for the high frequency PO_4 modes.

TABLE X. Infrared and silent vibrational modes of γ-Li_3PO_4 for $\nu > 0$, calculated using PWSCF and LDA exchange-correlation form using the same notation as in Table IX.

ν (cm^{-1})	Symmetry	Assignment	r
73	A_u	PO_4	1.9
105	B_{3u}	PO_4	1.8
191	B_{1u}	PO_4	1.6
197	A_u	PO_4	1.8
226	B_{2u}	PO_4	2.7
247	B_{1u}	PO_4	3.6
263	A_u	PO_4	1.7
272	B_{3u}	PO_4	3.9
323	B_{2u}	PO_4	2.8
331	B_{1u}	Li	0.17
331	A_u	Li	0.74
333	B_{3u}	Li	0.2
357	B_{2u}	Li	0.73
407	B_{1u}	PO_4	1.5
409	B_{1u}	Li	0.59
419	B_{2u}	Li	0.82
420	A_u	Li	0.75
426	B_{3u}	Li	0.53
434	B_{3u}	PO_4	1.9
453	B_{2u}	Li	0.74
457	B_{1u}	Li	0.54
464	A_u	Li	0.49
468	B_{3u}	Li	0.41
473	B_{2u}	Li	0.37
494	A_u	PO_4	1.4
500	B_{1u}	PO_4	1.2
504	A_u	Li	0.5
523	B_{3u}	Li	0.68
541	B_{1u}	Li	0.23
541	B_{2u}	Li	0.73
558	B_{3u}	Li	0.64
568	B_{3u}	PO_4	0.94
586	B_{1u}	PO_4	0.98
597	B_{2u}	PO_4	1.1
599	B_{3u}	PO_4	1.1
602	A_u	PO_4	1.2
628	B_{1u}	PO_4	1.1
938	B_{1u}	PO_4	5.5
943	B_{3u}	PO_4	4.4
1019	B_{2u}	PO_4	24
1026	B_{1u}	PO_4	32
1039	B_{3u}	PO_4	17
1054	A_u	PO_4	15
1068	B_{3u}	PO_4	25
1153	B_{1u}	PO_4	7.4

TABLE XI. Raman active vibrational modes of β-Li_3PO_4 calculated using PWSCF and LDA exchange-correlation form, with the same notation as in Table IX except that r is now defined by Eq. (A4).

ν (cm^{-1})	Symmetry	Assignment	r
159	A_2	PO_4	1.9
181	A_1	PO_4	2.2
184	A_2	PO_4	1.5
201	B_2	PO_4	4.5
232	A_1	PO_4	2.1
245	B_1	PO_4	2.7
252	B_2	PO_4	3.2
281	A_2	PO_4	4.0
321	B_1	PO_4	3.8
349	A_2	Li	0.73
355	B_2	Li	0.58
381	A_1	PO_4	0.96
388	B_1	PO_4	1.0
412	A_2	Li	0.69
412	A_1	Li	0.25
424	B_2	Li	0.31
428	B_1	Li	0.53
434	A_1	Li	0.37
448	A_2	Li	0.46
456	B_1	Li	0.25
465	B_2	PO_4	1.2
466	A_1	Li	0.57
472	B_1	Li	0.67
473	B_2	Li	0.74
494	A_2	Li	0.42
498	A_1	Li	0.73
513	A_1	Li	0.62
515	B_2	Li	0.65
522	A_2	PO_4	0.91
549	B_1	Li	0.78
559	B_2	Li	0.29
571	B_2	PO_4	1.7
579	A_1	PO_4	1.3
586	B_1	PO_4	1.6
609	B_2	PO_4	1.4
614	A_1	PO_4	1.2
630	A_2	PO_4	2.0
926	A_1	PO_4	17
936	B_2	PO_4	4.5
1013	B_1	PO_4	19
1020	A_1	PO_4	24
1024	A_1	PO_4	19
1045	B_2	PO_4	15
1050	B_2	PO_4	19
1060	A_2	PO_4	8.8

*duy@wfu.edu
†natalie@wfu.edu

[1] N. J. Dudney, in *Lithium Batteries: Science and Technology*, edited by G.-A. Nazri and G. Pistoia (Klumwer Academic, Dordrecht, 2004), Chap. 20, pp. 623–642.
[2] J. B. Bates, N. J. Dudney, G. R. Gruzalski, R. A. Zuhr, A. Choudhury, D. F. Luck, and J. D. Robertson, Solid State Ionics **53-56**, 647 (1992).
[3] J. B. Bates, N. J. Dudney, G. R. Gruzalski, R. A. Zuhr, A. Choudhury, D. F. Luck, and J. D. Robertson, J. Power Sources **43-44**, 103 (1993).
[4] B. Wang, B. C. Chakoumakos, B. C. Sales, B. S. Kwak, and J. B. Bates, J. Solid State Chem. **115**, 313 (1995).
[5] X. Yu, J. B. Bates, J. G. E. Jellison, and F. X. Hart, J. Electrochem. Soc. **144**, 524 (1997).
[6] Y.-W. Hu, I. D. Raistrick, and R. A. Huggins, J. Electrochem. Soc. **124**, 1240 (1977).
[7] R. A. Huggins, Electrochim. Acta **22**, 773 (1977).
[8] A. K. Ivanov-Shitz, V. V. Kireev, O. K. Mel'nikov, and L. N. Demainets, Crystallogr. Rep. **46**, 864 (2001).
[9] H. C. Liu and S. K. Yen, J. Power Sources **159**, 245 (2006).
[10] Y. A. Du and N. A. W. Holzwarth, J. Electrochem. Soc. **154**, A999 (2007).
[11] P. Hohenberg and W. Kohn, Phys. Rev. **136**, B864 (1964).
[12] W. Kohn and L. J. Sham, Phys. Rev. **140**, A1133 (1965).
[13] S. Baroni, A. Dal Corso, S. de Gironcoli, P. Giannozzi, C. Cavazzoni, G. Ballabio, S. Scandolo, G. Chiarotti, P. Focher, A. Pasquarello, K. Laasonen, A. Trave, R. Car, N. Marzari, and A. Kokalj, http://www.pwscf.org/
[14] D. Vanderbilt, Phys. Rev. B **41**, 7892 (1990); USPP code, http://www.physics.rutgers.edu/dhv/uspp/
[15] P. Tang, Ph.D. thesis, Wake Forest University, 2006.
[16] P. Tang, N. A. W. Holzwarth, and Y. A. Du, Phys. Rev. B (to be published 1 November 2007).
[17] J. P. Perdew and Y. Wang, Phys. Rev. B **45**, 13244 (1992).
[18] J. P. Perdew, K. Burke, and M. Ernzerhof, Phys. Rev. Lett. **77**, 3865 (1996); **78**, 1396(E) (1997).
[19] H. J. Monkhorst and J. D. Pack, Phys. Rev. B **13**, 5188 (1976).
[20] M. Parrinello and A. Rahman, J. Appl. Phys. **52**, 7182 (1981).
[21] A. Dal Corso, A. Pasquarello, and A. Baldereschi, Phys. Rev. B **56**, R11369 (1997).
[22] N. A. W. Holzwarth, A. R. Tackett, and G. E. Matthews, Comput. Phys. Commun. **135**, 329 (2001).
[23] A. R. Tackett, N. A. W. Holzwarth, and G. E. Matthews, Comput. Phys. Commun. **135**, 348 (2001).
[24] P. E. Blöchl, Phys. Rev. B **50**, 17953 (1994).
[25] H. Jónsson, G. Mills, and K. W. Jacobsen, in *Classical and Quantum Dynamics in Condensed Phase Simulations*, edited by B. J. Berne, G. Ciccotti, and D. F. Coker (World Scientific, Singapore, 1998), pp. 385–404.
[26] G. Henkelman, B. P. Uberuaga, and H. Jónsson, J. Chem. Phys. **113**, 9901 (2000).
[27] G. Henkelman and H. Jónsson, J. Chem. Phys. **113**, 9978 (2000).
[28] N. F. Mott and R. W. Gurney, *Electronic Processes in Ionic Crystals*, 2nd ed. (Dover, New York, 1965).
[29] D. M. Smyth, *The Defect Chemistry of Metal Oxides* (*Oxford University Press*, New York, 2000).
[30] G. Henkelman, Ph.D. thesis, University of Washington, 2001.
[31] A. Kokalj, J. Mol. Graphics Modell. **17**, 176 (1999).
[32] OPENDX, The Open Source Software Project Based on IBM's Visualization Data Explorer, http://www.opendx.org
[33] J. Zemann, Acta Crystallogr. **13**, 863 (1960).
[34] C. Keffer, A. Mighell, F. Mauer, H. Swanson, and S. Block, Inorg. Chem. **6**, 119 (1967).
[35] O. V. Yakubovich and V. S. Urusov, Crystallogr. Rep. **42**, 261 (1997).
[36] L. Popović, B. Manoun, D. de Wall, M. K. Nieuwoudt, and J. D. Comins, J. Raman Spectrosc. **34**, 77 (2003). Numerical values of the frequencies reported in this paper were obtained by manually digitizing the unlabeled peaks.
[37] R. M. Rojas, J. L. M. de Vidales, A. Delgado, and J. V. Sinisterra, J. Solid State Chem. **106**, 237 (1993).
[38] C. Ibarra-Ramírez, M. E. Villafuerte-Castrejón, and A. R. West, J. Mater. Sci. **20**, 812 (1985).
[39] R. J. Smith, Y. Shen, and K. L. Bray, J. Phys.: Condens. Matter **14**, 461 (2002).
[40] *International Tables for Crystallography, Volume A: Space-group symmetry*, 5th ed., edited by T. Hahn (Kluwer, Dordrecht, 2002).
[41] There is ambiguity in the literature in the choice of the **a**, **b**, and **c**, labels for the principle axes of γ and β-Li_3PO_4. Our choice is consistent with conventions given in Ref. 40.
[42] P. Tang and N. A. W. Holzwarth, Phys. Rev. B **68**, 165107 (2003).
[43] F. Harbach and F. Fischer, Phys. Status Solidi B **66**, 237 (1974).
[44] Y.-N. Xu, W. Y. Ching, and Y.-M. Chiang, J. Appl. Phys. **95**, 6583 (2004).
[45] B. N. Mavrin, V. V. Asonov, V. V. Fomichev, A. K. Ivanov-Shitz, and V. V. Kireev, J. Exp. Theor. Phys. **96**, 53 (2003).
[46] P. Tarte, J. Inorg. Nucl. Chem. **29**, 915 (1967).
[47] T. Riedener, Y. Shen, R. J. Smith, and K. L. Bray, Chem. Phys. Lett. **321**, 445 (2000).
[48] D. Morgan, A. V. der Ven, and G. Ceder, Electrochem. Solid-State Lett. **7**, A30 (2004).
[49] Chuying Ou-Yang, Siqi Shi, Z. Wang, X. Huang, and L. Chen, Phys. Rev. B **69**, 104303 (2004).
[50] W. Hayes and A. M. Stoneham, *Defects and Defect Processes in Nonmetallic Solids* (Wiley, New York, 1985).
[51] A. R. West, *Basic Solid State Chemistry*, 2nd ed. (Wiley, New York, 2000).
[52] Y. A. Du and N. A. W. Holzwarth (unpublished).
[53] H. Rabaâ, R. Hoffmann, N. C. Hernández, and J. F. Sanz, J. Solid State Chem. **161**, 73 (2001).
[54] D. L. Rousseau, R. P. Bauman, and S. P. S. Porto, J. Raman Spectrosc. **10**, 253 (1981).